Physics of Fluids

Vortex-induced vibrations of dual-step cylinders with different diameter ratios in laminar flows

Cite as: Phys. Fluids **31**, 073602 (2019); https://doi.org/10.1063/1.5097730
Submitted: 28 March 2019 . Accepted: 17 June 2019 . Published Online: 19 July 2019

Chunning Ji (及春宁), Yuting Cui (崔宇婷), Dong Xu (许栋), Xiaoxiao Yang (杨枭枭), and Narakorn Srinil

Physics of Fluids ARTICLE scitation.org/journal/phf

Vortex-induced vibrations of dual-step cylinders with different diameter ratios in laminar flows

Cite as: Phys. Fluids 31, 073602 (2019); doi: 10.1063/1.5097730
Submitted: 28 March 2019 • Accepted: 17 June 2019 •
Published Online: 19 July 2019

Chunning Ji (及春宁),[1,2] Yuting Cui (崔宇婷),[1] Dong Xu (许栋),[1,a)] Xiaoxiao Yang (杨枭枭),[1] and Narakorn Srinil[3]

AFFILIATIONS

[1]State Key Laboratory of Hydraulic Engineering Simulation and Safety, Tianjin University, Tianjin 300072, China
[2]Collaborative Innovation Centre for Advanced Ship and Deep-Sea Exploration, Shanghai 200240, China
[3]School of Engineering, Newcastle University, NE1 7RU Newcastle Upon Tyne, United Kingdom

[a)]Author to whom correspondence should be addressed: xudong@tju.edu.cn

ABSTRACT

Vortex-induced vibrations of dual-step cylinders in laminar flows at the Reynolds number of 200 based on a larger diameter are investigated through three-dimensional direct numerical simulations. Four larger-to-smaller diameter ratios (D/d) of 4.0, 2.0, 1.43, and 1.19 are considered for the cylinder with a low mass ratio of 2. Numerical results reveal that D/d significantly influences vibration responses and the vortex shedding process. The case with D/d = 1.43 can effectively reduce vibration amplitudes. The wake vortices are shed in cellular patterns along the cylinder span, with a distinct frequency for each cell. A direct and "X-shaped" connection of wake vortex-shedding modes occurs between different vortex cells, and a loop connection appears between the same cell vortices. A new wake pattern entitled the "out-of-phase vortex shedding" is found downstream of the smaller cylinder at D/d = 2.0. This is manifested by the wake vortices not being shed at a fixed frequency and intensity. The essential reason for this phenomenon lies in a non-lock-in condition between the structural vibration and vortex shedding frequencies of the smaller cylinder. As D/d decreases, a coherence between vortex cells is enhanced, leading to a disappearance of the "out-of-phase vortex shedding."

I. INTRODUCTION

Vortex-induced vibration (VIV) of circular cylinders or bluff bodies is encountered in various engineering problems such as civil structures, mechanical engineering systems, and ocean engineering platforms. Since VIV may cause serious damage to structures, it has been a topic of intense study for a long time, and these studies[1–7] have revealed some essential characteristics of VIV. When the vortex shedding frequency of the cylinder is synchronized with the structural vibration frequency, a so-called lock-in phenomenon occurs. This lock-in can occur within a certain incoming flow velocity range, during which the shedding frequency deviates from the Strouhal frequency, and large vibration amplitude can be excited, which can lead to structural fatigue and earlier failure. Govardhan *et al.*[2–4] reported that a different mass-damping parameter $m^*\zeta$ can result in two distinct kinds of vibration responses for the elastically supported cylinder. At high $m^*\zeta$, initial and lower response branches appear, with the maximum amplitude occurring at the initial branch. At low $m^*\zeta$, three different response branches exist, including initial, upper (or super-upper), and lower branches, with the maximum amplitude corresponding to the upper branch. However, the investigation at low Reynolds (Re) number in the 60 < Re < 200 range performed by Prasanth and Mittal[5–7] showed that there are only initial and lower branches found in the cylinder response, and the maximum amplitude appears in the lower branch. In addition, a series of wake vortex shedding modes such as 2S, 2P, 2T, and P+S is found,[8–12] reflecting a coupling between the wake vortices and the cylinder response in different response branches. A comprehensive review of related research can be found in the work of Williamson and Govardhan.[1] Recent progress includes predicting VIV by using a deep learning,[13] coupling VIV with thermal dynamics,[14] and suppressing VIV by using a complex geometry.[15]

In recent years, complex cylindrical structures evolve with nonuniform geometries in real-life engineering practice such as marine risers with a series of intermediate buoyancy modules. Due to a discontinuity in the diameters (the larger and smaller

cylinders have diameters of D and d, respectively), the flow field and wake vortex characteristics of such a stepped cylinder are significantly different from those of a uniform cylinder. To date, a majority of previous studies have focused on the fluid forces and wake patterns of a fixed stepped cylinder. Norberg[16] observed a special vortex shedding frequency behind the step, which is lower than those of the larger and smaller cylinders. Lewis and Gharib[17] classified the wake modes of a single-step cylinder at different diameter ratios (D/d) at low Re = 35–200. When $D/d < 1.25$, a direct wake mode occurs, accompanied by two distinct vortex-shedding frequencies behind the larger and smaller cylinders, respectively. The vortices shed from both cylinders are directly connected, interacting in a narrow region downstream the step. When $D/d > 1.55$, there appears an indirect wake mode. A third frequency, besides the shedding frequencies of the larger and smaller cylinder, exists behind the step on the larger cylinder side. A region where this frequency appears is called the frequency-modulated region in which vortices with different shedding frequencies interact and adjust. When $1.25 < D/d < 1.55$, the wake shows a transition mode. Based on the different shedding frequencies appearing behind the single-step cylinder in the indirect mode, Dunn and Tavoularis[18] classified the spanwise vortex cells of the singe-step cylinder into three categories: the vortices shed from the smaller cylinder, the larger cylinder, and the step are the S-cell, L-cell, and N-cell, respectively. The S-cell has the highest shedding frequency, and the frequencies of the L- and N-cells are sequentially decreased. Owing to the difference in the shedding frequency of vortex cells, a variety of vortex interactions occur within vortex cells and at the cell boundaries, such as the half-loop connections between the two vortices of the opposite sign within one cell and the direct cross-boundary connections between the two different vortex cells. At the same time, two streamwise vortex structures, the junction vortex and the edge vortex rotating in the opposite directions at the root of the smaller cylinder, were observed in their study. Morton and Yarusevych[19] simulated the vortex shedding of a single-step cylinder. Their results showed that a transition region at the N-S cell boundary is narrow, and the vortex dislocations represent the half-loop connection of the two opposite-phase vortices in the S-cell. However, the transition region at the N-L cell boundary is wider and its spanwise extent fluctuates in time.

Williamson[20] attached a ring with $1.5D$ in diameter and $0.5D$ in length to a circular cylinder with a diameter of D, forming a dual-step cylinder artificially. His results showed that this ring disturbance can cause vortex dislocations to appear on each side of the ring, and by deliberately controlling the vortex shedding frequencies on each side of the ring, the two-sided vortex dislocations can be in- or out-of-phase. In addition, due to the different dislocation frequencies on each side, the out-of-phase two-sided dislocation is a transient phase relationship between the two dislocations, but the in-phase two-sided dislocation with the same dislocation frequency is stable. Morton and Yarusevych[21] carried out a detailed study on the effect of different aspect ratios ($0.2 \le L/D \le 17$ with L being the spanwise length of the larger cylinder) on the wake vortex of a dual-step cylinder at $Re_D = 1050$. Their work showed that the wake vortices are closely related to L/D. Four distinct vortex shedding modes are identified: (i) when $L/D \ge 15$, three obvious vortex shedding (S, N, and L) cells appear behind the larger cylinder, and the vortex dislocations periodically occur between vortex cells; (ii) when $8 \le L/D \le 14$, there is only L-cell in the larger cylinder wake and its frequency decreases with decreasing L/D; (iii) when $2 \le L/D \le 6$, the larger cylinder vortices undergo severe deformation in the near wake and the vortex shedding has a high degree of three-dimensionality; and (iv) when $0.2 \le L/D \le 1$, obvious periodic velocity fluctuations can be observed in the wake of the larger cylinder, the frequency increases with decreasing L/D, but there is no periodic wake structure behind the larger cylinder. McClure *et al.*[22] numerically investigated a flow development over dual step cylinders for $1.1 \le D/d \le 4$ and $0.2 \le L/D \le 5$ and found that these two geometric parameters have a significant effect on the wake topology. When changing D/d and L/D, distinct types of wake patterns and interactions between larger and smaller cylinders' vortices appear. They also clarified two important frequencies in the periodic vortex interactions, namely, the beat frequency ($f_S - f_L$) and the fundamental dislocation frequency (f_{FD}), where f_S and f_L are the vortex-shedding frequencies of the S and L cells, respectively. Morton and Yarusevych[23] studied experimentally the effects of L/D ($0.2 \leqslant L/D \leqslant 3$) and Re ($Re_D = 1050$ and 2100) on the dual step cylinder wake development. At low L/D, the vortex shedding behind the larger cylinder is weak and the dominant frequency in the larger cylinder wake is caused by the passage of vortex filaments connected to the smaller cylinder's vortices. The existence of the larger cylinder at these low L/D gives rise to the periodic vortex dislocations. When increasing L/D, vortex dislocations occur more frequently and the dominant frequency downstream the larger cylinder decreases. In addition, Re has a more profound effect on the wake vortex of the dual step cylinder than that of the uniform cylinder. Morton and Yarusevych[24] also carried out an experimental study on three-dimensional characteristics of the dual step cylinder wake, covering a wide range of Re, L/D, and D/d. They identified four distinct wake regimes according to the vortex shedding of the larger cylinder. It is worth mentioning that they successfully introduced and applied a POD-based phase averaging method to reconstruct the dominant coherent structures and estimate their phase variations.

When such a stepped cylinder undergoes VIV, a significant shedding frequency difference will occur due to the discontinuity of diameters along the span,[25] compared with VIV of a uniform cylinder. This makes it possible for spanwise positions with different diameters to be on different response branches. In addition, there might be a complex vibration response in which the region with one diameter is non-locked-in, while the region at the other diameter is locked-in. However, understanding of this topic still remains incomplete. For this reason, we numerically study VIV of a dual-step cylinder with four different D/d, for which the cylinder is free to vibrate in both in-line and cross-flow directions. The objective of the present work is to reveal the influence of variable D/d on the cylinder vibration response, with emphasis on the coupling mechanism between the cylinder vibration and wake vortices, so as to provide a deeper insight answering the following questions: (i) What are the main different characteristics of VIV of dual-step vs uniform cylinders? (ii) Whether the lock-in or non-lock-in region appears in different positions along the cylinder span? (iii) How D/d influences VIV of dual-step cylinders? (iv) What are the vortex-shedding modes? and (v) How the vortex shedding process and structural vibration do couple?

The rest of the paper is organized as follows. The numerical method is presented in Sec. II. The cylinder vibrations and

mechanisms of the wake vortex shedding are investigated in Sec. III. Key conclusions are summarized in Sec. IV.

II. NUMERICAL METHODOLOGY

A. Numerical formulation

The fluid-structure interaction (FSI) in the present study is simulated by using the immerse boundary (IB) method first introduced by Peskin.[26] In the IB framework, the fluid governing equations are discretized on a fixed Cartesian grid, which does not distort with the motion and geometric deformation of the structure. In this case, the boundary conditions on the fluid-structure interface which reflect the FSI cannot be imposed directly. Instead, an extra body force is added to the momentum equations by using the interpolation and distribution functions to take such an interaction into account.

The conservative form of the second-order Adams-Bashforth temporal-discretized governing equations of incompressible fluid flow using the IB method is

$$\mathbf{u}^{n+1} = \mathbf{u}^n + \delta t\left(\frac{3}{2}\mathbf{h}^n - \frac{1}{2}\mathbf{h}^{n-1} - \frac{3}{2}\nabla p^n + \frac{1}{2}\nabla p^{n-1}\right) + \mathbf{f}^{n+\frac{1}{2}}\delta t, \quad (1)$$

$$\nabla \cdot \mathbf{u}^{n+1} = 0, \quad (2)$$

where $\mathbf{u}$ is the velocity, p is the pressure, $\mathbf{h} = \nabla\cdot(-\mathbf{uu} + \nu(\nabla\mathbf{u} + \nabla\mathbf{u}^t))$ comprises the convective and diffusive terms, ∇ denotes the gradient operator, a superscript t is the matrix transposition, and superscripts $n+1$, $n+1/2$, n, and $n-1$ indicate the time step. $\mathbf{f}$ denotes the extra body force which is calculated as

$$\mathbf{f}^{n+\frac{1}{2}}\delta t = D\left(\mathbf{F}^{n+\frac{1}{2}}\right) = D\left\{\mathbf{V}^{n+1} - I\left[\mathbf{u}^n + \delta t\left(\frac{3}{2}\mathbf{h}^n - \frac{1}{2}\mathbf{h}^{n-1} - \frac{3}{2}\nabla p^n + \frac{1}{2}\nabla p^{n-1}\right)\right]\right\}, \quad (3)$$

where $\mathbf{F}$ is the extra body force on IB points and $\mathbf{V}$ is the desired velocity of IB points obtained by solving the governing equations of cylinder motions [Eqs. (4) and (5)]. $I(\varphi, \mathbf{X}_i)$ and $D(\Phi, x)$ are the smoothed discrete delta functions developed by Yang *et al.*[27] to reduce the nonphysical force oscillations when handling the moving solids. The two-step predictor-corrector procedure is adopted for decoupling the flow governing equations [Eqs. (1)–(3)]. The resultant pressure Poisson equation is solved by using the biconjugate gradient stabilized method BiCGSTAB,[28] preconditioned by using the geometric multigrid method. For the sake of conciseness, the detailed methodology can be found in our previous work[29] for further information.

The equations of motions of the elastically mounted dual-step cylinders in in-line and cross-flow directions are expressed as follows:

$$m\frac{d^2x}{dt^2} + c\frac{dx}{dt} + kx = F_x, \quad (4)$$

$$m\frac{d^2y}{dt^2} + c\frac{dy}{dt} + ky = F_y, \quad (5)$$

where m is the structural mass, c is the structural damping, and k is the stiffness constant. The above equations are solved by applying the standard Newmark-β method. For exciting larger vibration amplitudes of the cylinder, c is set as zero in the present study.

TABLE I. Grid convergence study for dual-step cylinders at $\mathrm{Re}_D = 200$ and $U_r = 5.0$.

Mesh	$\Delta x/D$ (=$\Delta y/D$)	$A_{y,max}$	$C_{D,mean}$	$C_{L,rms}$
A	1/16	0.559 (9.1%)	1.352 (5.4%)	0.287 (64.7%)
B	1/32	0.509 (−0.6%)	1.271 (−0.9%)	0.189 (8.6%)
C	1/64	0.512	1.283	0.174

k is determined by setting the reduced velocity $U_r = U_\infty/f_nD$, where $f_n = 1/2\pi\sqrt{k/m}$ is the cylinder natural frequency and U_∞ is the unaffected incoming flow velocity. To couple fluid flow and cylinder motion, in-line and cross-flow fluid forces (F_x and F_y) are calculated as the integral of $\mathbf{F}$ on the fluid-structure interface, while the desired velocity $\mathbf{V}$ in Eq. (3) is calculated as $[dx/dt, dy/dt]$, obtained by solving Eqs. (4) and (5).

B. Grid convergence study and validation cases

To verify the independency of numerical results on the mesh density, simulations are conducted at three meshes with different densities as shown in Table I for VIV of dual-step cylinders with $D/d = 2.0$, $L/D = 10.0$ (see the geometry in Fig. 1) and $m^* = 2.0$ at $\mathrm{Re}_D = 200$ and $U_r = 5.0$. Cylinder responses and associated hydrodynamic force coefficients are presented. With mesh C being the reference, the differences between results from mesh A or B and those from mesh C are reported in the brackets. It can be seen from Table I

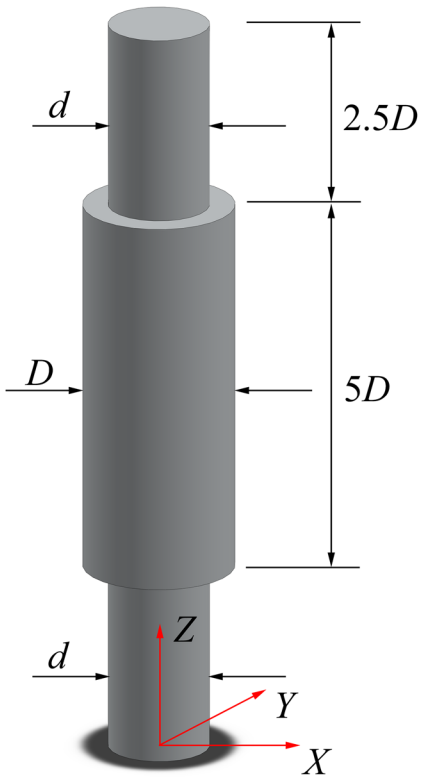

FIG. 1. Dual-step cylinder geometry.

TABLE II. Comparison of VIV simulation results of a uniform cylinder at Re = 100.

	$A_{y,max}$	$C_{D,mean}$	$C_{D,rms}$	$C_{L,rms}$	St
Present	0.522	1.910	0.250	0.155	0.164
Prasanth and Mittal[5]	0.516	1.900	0.255	0.148	0.164
Difference (%)	1.16	0.53	1.96	4.73	0.00

that differences in cross-flow amplitudes $A_{y,max}$ and mean drag force coefficients $C_{D,mean}$ between meshes B and C are within 1%. The difference in rms lift force coefficient $C_{L,rms}$ between meshes B and C is greatly reduced when compared to mesh A. This indicates that results from mesh C are convergent and grid-independent. Therefore, mesh C is selected for numerical simulations in the present study.

To verify accuracy of the numerical methodology, VIV of a uniform cylinder with $m^* = 10$ at Re = 100 in the computational domain $[-25D, 25.5D] \times [-10D, 10D]$ is simulated. This domain and the simulation parameters are chosen to be the same as those in the work of Prasanth and Mittal.[5] Table II compares the present simulation results with the results of Prasanth and Mittal. It can be seen that a good agreement is achieved for the vibration displacement amplitude, fluid force coefficients, and Strouhal numbers. The maximum difference in $C_{L,rms}$ is about 4.73%, within a reasonable error range.

III. RESULTS AND DISCUSSION

As shown in Fig. 1, the dual-step cylinder geometry of interest consists of two different diameters, with a 5D long larger diameter (D) cylinder attached coaxially at the midspan of a 10D long smaller diameter (d) cylinder. Four different D/d = 1.19, 1.43, 2.0, and 4.0 are adopted with D being fixed while d being varied. Re_D is 200, while Re_d changes with D/d. $m^* = 2.0$ and $U_r = 5.0$ are fixed for the purpose of exciting large-amplitude vibrations at resonance, considering $St \approx 0.2$ at Re = 200. The geometry of the dual-step cylinder follows that of a typical marine riser fitted by a buoyancy module with a coverage of 50%.

The calculational domain in in-line (X), cross-flow (Y), and spanwise (Z) directions is set as $70D \times 50D \times 10D$, respectively. The center of the cylinder is separated from the inflow boundary ($-X$), the outflow boundary ($+X$), and the upper and lower boundaries ($\pm$Y) by 20D, 50D, and 25D, respectively. A uniform mesh with a grid spacing of $\Delta x = \Delta y = D/64$ in the X–Y plane is applied in a square region of $8D \times 4D$ around the cylinder to ensure the simulation accuracy. Outside this region, a stretched mesh is adapted by keeping the total number of grids within an affordable range. Along the cylinder span, a uniform mesh is adopted with a grid spacing of $\Delta z/D = 1/19.2$. The grid resolution is 768 × 512 × 192 in the in-line, cross-flow, and spanwise directions. The Dirichlet and Neumann boundary conditions are imposed at the inflow and outflow, whereas the free slip and periodic conditions are adopted at the transverse and spanwise boundaries, respectively. The cylinder is nonslip and impermeable. In order to satisfy the CFL condition ($U_\infty \Delta t/\Delta x < 0.5$), the normalized time step size is $\Delta t U_\infty/D = 0.006$.

Prior to discussing simulation results, it is necessary to briefly describe the wake vortices of the dual-step cylinders when VIV occurs, providing a visual impression. In so doing, vortices are visualized by the isosurfaces of $\lambda_2 = -0.1$, being the second largest eigenvalue of the symmetric tensor $\mathbf{S}^2 + \mathbf{\Omega}^2$, where $\mathbf{S}$ and $\mathbf{\Omega}$ are, respectively, the symmetric and asymmetric parts of the velocity gradient tensor $\nabla \mathbf{u}$. The color on the isosurfaces indicates the vorticity in the spanwise direction. The analysis of vortex shedding of the dual-step cylinder follows the terminology defined by Dunn and Tavoularis,[18] as shown in Fig. 2. The spanwise vortex units behind the larger and smaller cylinders are the L-cell and the S-cell, respectively, and vortices in different cells are connected by either the direct cross-boundary or "X-shaped" connections depending on the phase differences between vortex cells. There are also the paired streamwise vortices at the steps, which are the edge vortices formed when the streamlines flow over the step edge and the junction vortices at the root of the smaller cylinder. In addition, the center vortices appear near the center of the larger cylinder, as indicated by the solid lines in Fig. 2. Compared with the wake vortices when the dual-step cylinder is stationary, no obliquely shedding N-cell[17,18,22] is found when VIV occurs, and the half-loop connection is not formed between S-cell vortices.

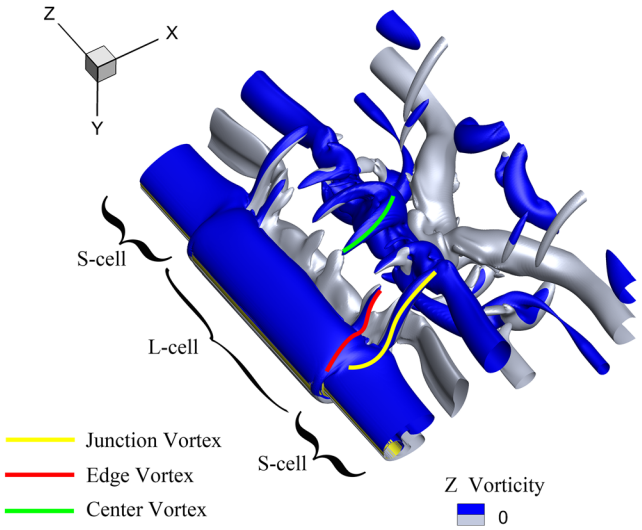

FIG. 2. Different vortex cells in the wake of dual-step cylinder with D/d = 2.0. Vortices are visualized by the isosurfaces of $\lambda_2 = -0.1$ and colored by the Z-vorticity.

A. Cylinder vibration characteristics

Figure 3 displays a temporal evolution of displacement responses of dual-step cylinders at four D/d. It is found that the cross-flow displacement amplitude is much larger than the in-line counterpart. When D/d = 2.0, the cylinder exhibits a beating-like vibration in the in-line direction, while the cases with D/d = 4.0, 1.43, and 1.19 show regular single-frequency vibrations. The passive suppression effect of the step change on VIV is one of the concerns in the present study. Table III summarizes cross-flow amplitudes A_y at different D/d vs those of a uniform cylinder with diameter D. The differences between the results of dual-step and uniform cylinders are also listed. It can be seen that VIV of dual-step cylinders can

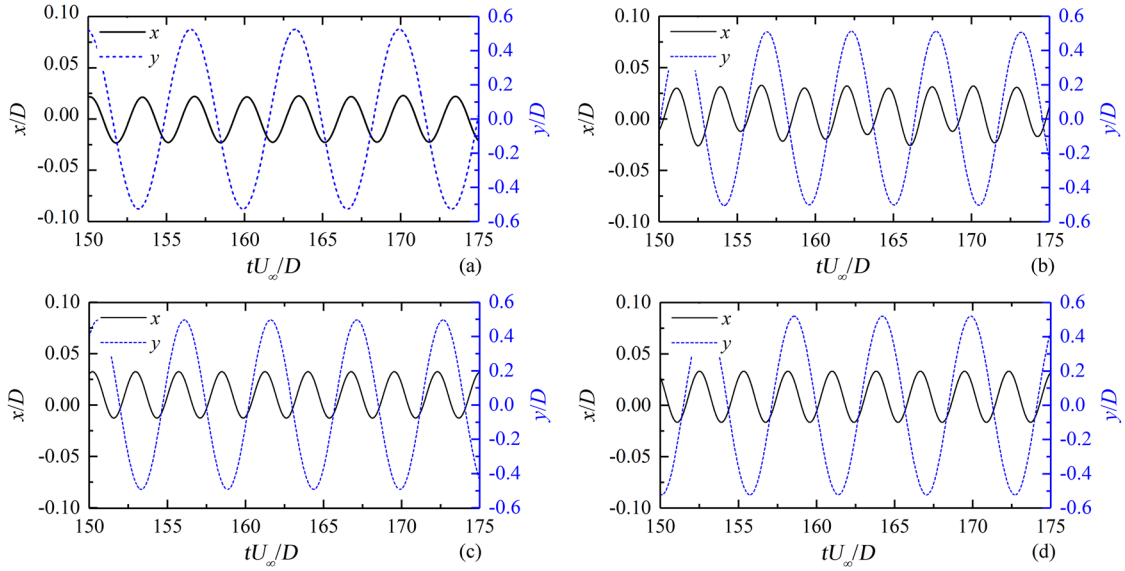

FIG. 3. Time histories of in-line and cross-flow displacements at different D/d: (a) D/d = 4.0, (b) D/d = 2.0, (c) D/d = 1.43, and (d) D/d = 1.19.

be effectively diminished by the steps, and the reduction is more significant in the case of D/d = 1.43 than that of D/d = 4.0, 2.0, and 1.19.

The vibration trajectories, frequencies, and phase differences between in-line and cross-flow displacements of the dual-step cylinder at four different D/d are plotted in Fig. 4. The trajectories are obtained by selecting the steady-state displacements for which mean values of the streamwise offset have been subtracted. The oscillation frequencies are calculated by using the fast Fourier transform. The instantaneous phases φ_x and φ_y of in-line and cross-line vibrations are determined by means of the Hilbert transform, and the phase difference is evaluated by $\varphi_{xy} = [p\varphi_x - q\varphi_y, \text{mod } 360^\circ]$, as suggested in the work of Bourguet *et al.*,[30] where $p = 1$ and $q = 2$ are the two integer numbers defining the level of synchronization. Bourguet *et al.*[30] have shown that values of the x-y phase difference (φ_{xy}) in the range of 0°–180° and 180°–360° correspond to the counterclockwise and clockwise "figure-of-eight" trajectories, respectively. Such a relation is also observed for the four D/d cases herein. For example, comparing the cases of D/d = 4.0 and 2.0, the mean phase differences $\overline{\varphi}_{xy}$ are 334° and 41°, respectively, corresponding to trajectories in the opposite rotation direction. Due to the beatinglike vibration existing in the in-line direction at D/d = 2.0, the resultant "figure-of-eight" trajectories in several periods cannot completely coincide. Upon closer inspection, such beating is found to be mainly manifested by the cylinder's upstream movement: the upstream amplitude fluctuates between 0.018 and 0.032, as illustrated in Fig. 4(b), region I. However, there is no a significant beating when the cylinder moves downstream, as illustrated in Fig. 4(b), region II. From the spectrum of the in-line displacement (x) at D/d = 2.0, the multipeak pattern is observed with the largest peak at f = 0.372 and a smaller peak at f = 0.149. The dominant frequency f = 0.372 is caused by the spanwise vortex-shedding, while the occurrence of f = 0.149 is related to the streamwise vortex structures at the steps and the time-varying S-cell downstream of the smaller cylinder. This is discussed in detail in the following wake analysis. In addition, a frequency with a much lower intensity f = 0.223 appears in the in-line displacement spectrum, and this can be taken as the beating frequency of the above two frequencies. By comparing with the multipeak spectral plot of the in-line vibration, the cross-flow vibration frequency shows only one peak at f = 0.186. It is seen that the in-line dominant frequency is twice the cross-flow dominant frequency, which often characterizes the uniform cylinder.[1] This dual-resonance relationship can also be observed at other three D/d, but the beating in-line vibration and the corresponding multipeak spectrum are absent. Moreover, the vibration frequencies in both directions are slightly reduced as D/d is smaller than 2.0. When D/d = 4.0, an opposite change occurs, and the vibration frequency at this time is smaller than that of D/d = 2.0. Concerning the uniform cylinder (D/d = 1.0), a "figure-of eight" trajectory also appears and the phase difference fluctuates approximately between 20° and 80° with a mean value of $\overline{\varphi}_{xy}$ = 51°. Overall, it can be summarized from the above comparison that the dual-step cylinders affect the phase difference between in-line and cross-flow vibrations and further controls the specific shape of orbital motions.

TABLE III. Cross-flow amplitude (A_y) at different D/d. A comparison of results between dual-step and uniform cylinders is also shown.

D/d	A_y	Difference (%)
4.00	0.528	−14
2.00	0.513	−16
1.43	0.496	−19
1.19	0.529	−14
1.00	0.612	...

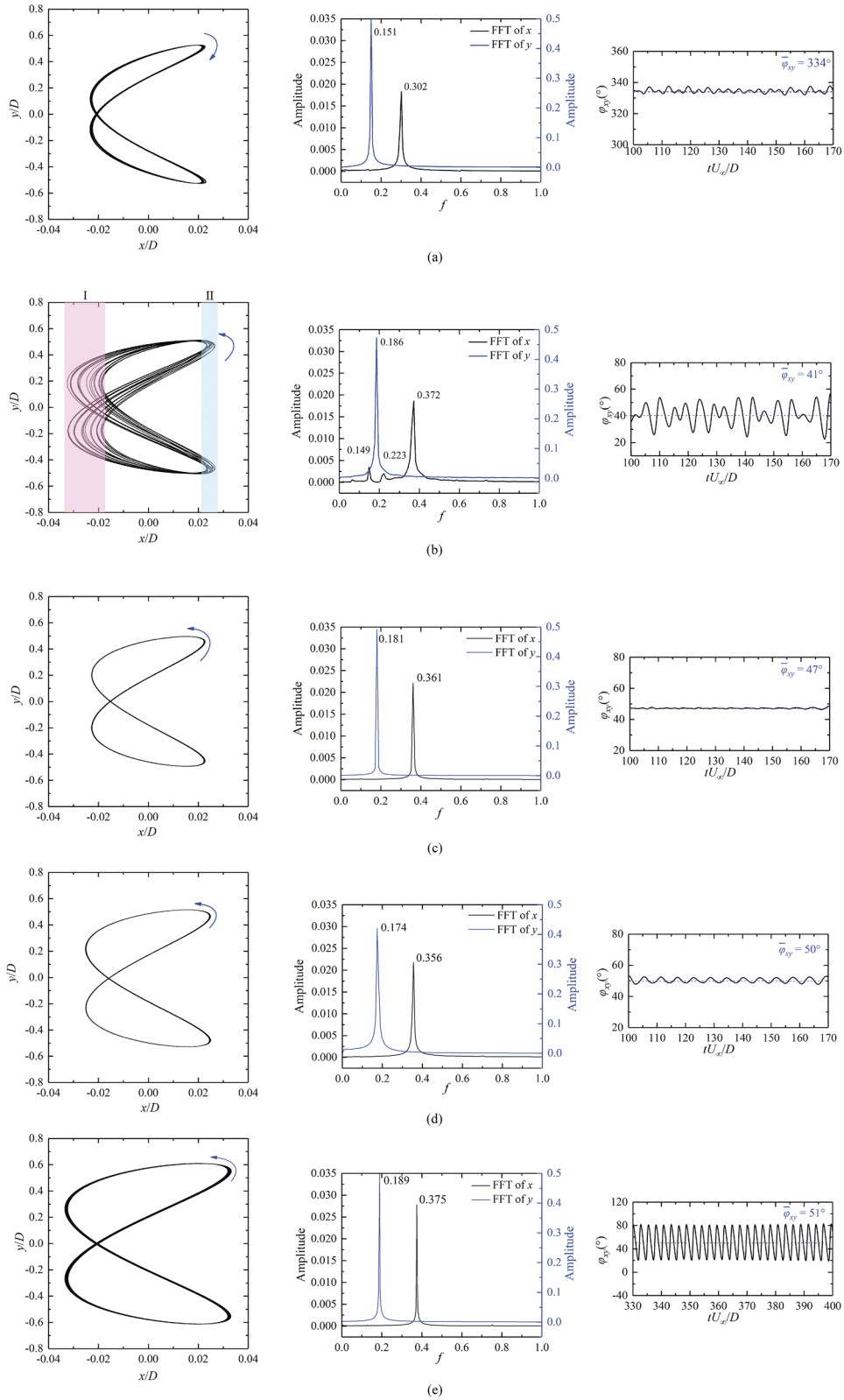

FIG. 4. Vibration trajectories, frequencies, and phase differences (φ_{xy}) between in-line and cross-flow vibrations of dual-step cylinders at different D/d: (a) D/d = 4.0, (b) D/d = 2.0, (c) D/d = 1.43, (d) D/d = 1.19, and (e) D/d = 1.0.

B. Time-space distributions of velocity fluctuations

Since vortices are shed alternatively on both sides of the cylinder, an appropriate cross-flow offset can obtain more sufficiently the wake information when arranging a measuring line along the cylinder span. The present study follows the arrangement in the study of McClure *et al.*,[22] where a measuring line is arranged at $X/D = 5$ and $Y/D = 0.75$ (at the cylinder origin), and the space-time distributions of the velocity fluctuations in three directions are obtained in Fig. 5. By taking any time after the vortex-shedding stabilization as the starting point, the evolution in $\Delta tU_\infty/D = 80$ is counted.

When $D/d = 4.0$, the velocities in all three directions regularly fluctuate. In in-line and cross-flow directions, different velocity fluctuations (u' and v') occur behind larger and smaller cylinders. In the spanwise velocity fluctuations w', it is found that there exists a

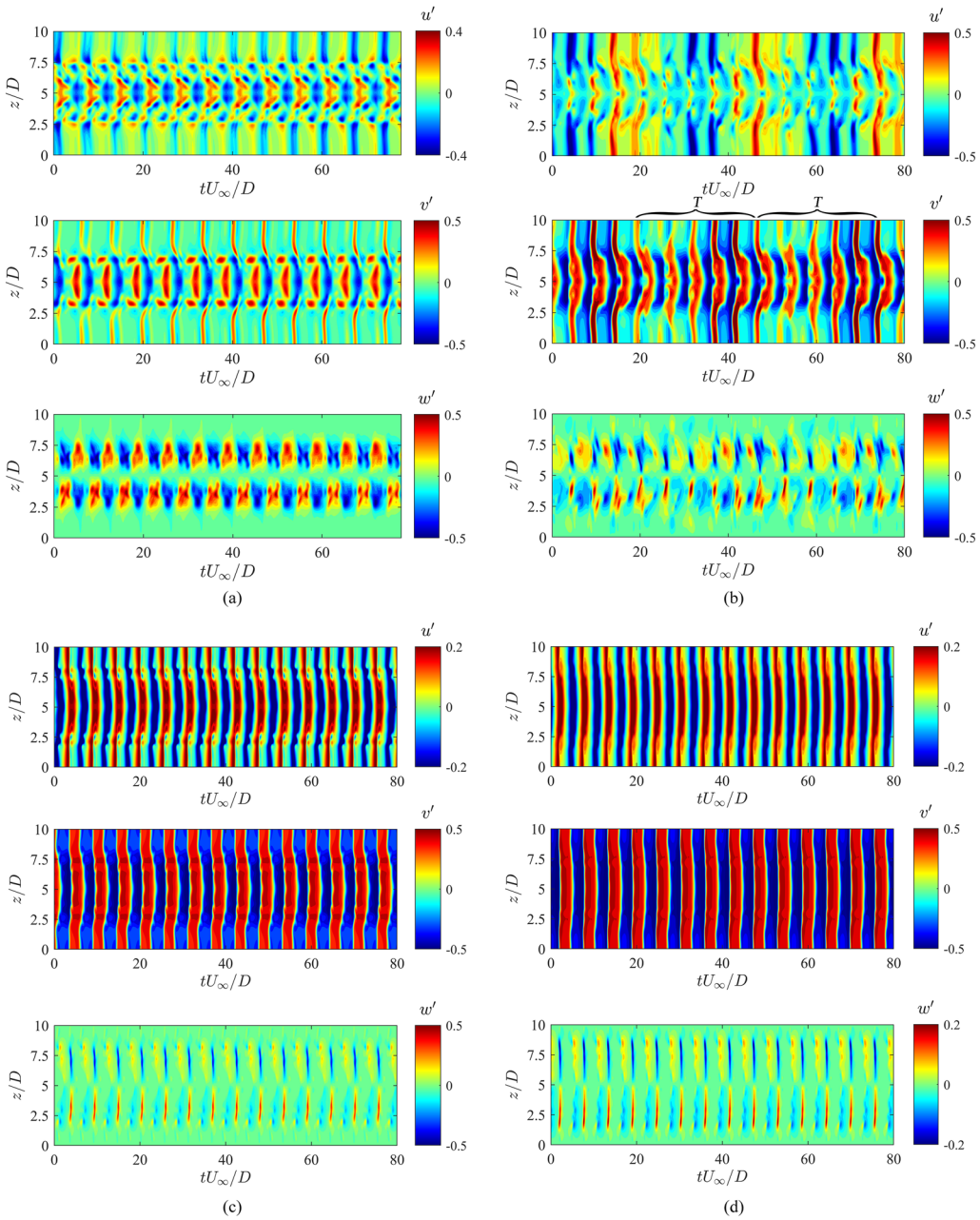

FIG. 5. Time-space distributions of velocity fluctuations in three directions at $X/D = 5$ and $Y/D = 0.75$ for four different D/d: (a) $D/d = 4.0$, (b) $D/d = 2.0$, (c) $D/d = 1.43$, and (d) $D/d = 1.19$.

spanwise flow with alternating directions between the center of the larger cylinder and the steps. For the step cylinder, as fluid separates over the sharp edge of the step, it will be deflected spanwise into the larger cylinder wake and generates a form of downwash, which was observed in the work of Dunn and Tavoularis.[18] It is apparent in Fig. 5(a) that the spanwise flow appears with a longer duration and greater intensity at $D/d = 4.0$ when compared to other D/d cases, revealing that there is indeed a substantial downwash fluctuation near the step.

For $D/d = 2.0$, a complex in-line velocity fluctuation u' occurs: the inconsistent velocity fluctuations exhibit behind both larger and smaller cylinders. For example, at $tU_\infty/D = 36$, the negative and positive fluctuations appear downstream of the smaller cylinder and the center of the larger cylinder, respectively, and simultaneously. For the cross-flow velocity fluctuation v', two periods consisting of the above complex velocity fluctuations appear continuously in the range of $tU_\infty/D = 20$–74, as indicated by "T" in Fig. 5(b). The period of one complete cycle is about $tU_\infty/D = 27$, corresponding to a frequency of $f = 1/27 = 0.037$. Furthermore, the spanwise flow also exhibits a significant change in strength and duration, indicating that different vortex cells of the dual-step cylinder have inconsistent interactions at different instants.

When $D/d = 1.43$ and 1.19, the velocity fluctuations in in-line and cross-flow directions (u' and v') are regular throughout the whole cylinder span, without an obvious low frequency fluctuation. Similar to that at $D/d = 2.0$, a significant spanwise flow can still be observed, but these two D/d cases exhibit a relatively stable and regular change. In addition, the range of the spanwise flow at $D/d = 1.19$ extends downstream of the smaller cylinder, which is significantly larger than those with $D/d = 4.0$, 2.0, and 1.43.

C. Velocity spectra

Power spectral densities (PSDs) of the velocity fluctuations along the measuring line are presented in Fig. 6. In the present study, the nondimensional frequency f is normalized by U_∞/D. When $D/d = 4.0$, the dominant shedding frequency behind the larger cylinder is $f = 0.151$ in the in-line and cross-flow velocity fluctuation spectra (PSD-u' and PSD-v'), consistent with the cylinder vibration frequency. In addition, there is a significant second-order frequency $2f = 0.302$ appearing downstream of the step and on the larger cylinder side. This distinct frequency is related to the loop connection between two consecutive L-cell vortices behind the larger cylinder as will be illustrated clearly in Subsection III D. For downstream of the smaller cylinder, $f = 0.151$ and its high-order frequencies $2f = 0.151$, $3f = 0.453$, and $4f = 0.604$ are scattered. Since the shedding frequency of the smaller cylinder is exactly an integral multiple of that of the larger cylinder, $f = 0.151$ behind the smaller cylinder corresponds to the frequency of the vortex-shedding phase readjustment period of the small cylinder. In the spanwise velocity fluctuation spectrum (PSD-w'), there is only a significant frequency distribution behind the larger cylinder owing to a weak spanwise flow behind the smaller cylinder.

A more scattered frequency distribution occurs when $D/d = 2.0$. In the in-line velocity fluctuation spectrum (PSD-u') at $D/d = 2.0$, two prominent frequencies $f = 0.149$ and 0.186 appear downstream of the larger cylinder, where $f = 0.186$ is the vortex shedding frequency of the L-cell behind the larger cylinder and $f = 0.149$ matches the low in-line vibration frequency. However, $f = 0.149$ does not appear behind the smaller cylinder: this is attributed to the time-varying S-cell of the small cylinder which will be explained later. At the downstream of the smaller cylinder, a dominant low frequency $f = 0.037$ appears, which is essentially the occurrence frequency of the long period variation of the velocity fluctuation, as discussed in Subsection III B. Other weaker frequencies, such as $f = 0.186$, $f = 0.223$, and $f = 0.258$, appear scattered in the spectrum behind the smaller cylinder. Therein, $f = 0.186$ is the shedding frequency of the S-cell directly connected with the L-cell, whereas $f = 0.223$ and $f = 0.258$ are related to the strong S-cell of the smaller cylinder. This will be also explained later.

In the cross-flow velocity fluctuation spectrum (PSD-v'), the dominant vortex shedding frequency behind the larger cylinder is $f = 0.186$. At the downstream of the smaller cylinder, three comparable frequencies $f = 0.223$, 0.407, and 0.437 are apparent, where $f = 0.407$ is the vortex shedding frequency of the S-cell behind the smaller cylinder. Such three frequencies downstream the smaller cylinder are different from the cylinder vibration frequency ($f = 0.186$), indicating that there is no synchronization between the vortex shedding of the smaller cylinder and the structural vibration. For PSD-w', there is only a significant frequency distribution on the larger cylinder side, and the frequency behind the smaller cylinder is not obvious. Same frequencies $f = 0.037$, 0.186, 0.336, 0.372, and 0.407 appear with $f = 0.186$ prevailing.

When $D/d = 1.43$, the distributions of the velocity fluctuation spectra of the larger and smaller cylinders are highly consistent, and the dominant shedding frequency $f = 0.181$ can be observed in all three directions. Moreover, the dominant shedding frequency is equal to the vibration frequency (see Fig. 4), showing that the vortex shedding and structural frequencies are locked along the whole cylinder span. In addition, high-order harmonics appear to be meaningful in the velocity spectra in three directions, i.e., $2f = 0.358$, $3f = 0.542$, and $4f = 0.724$. The spectra of the velocity fluctuations at $D/d = 1.19$ reveal similar characteristics, and the dominant frequency is $f = 0.174$.

D. Wake vortices

Figure 7 illustrates the instantaneous isosurfaces of λ_2 at two instants with $D/d = 1.19$ and 1.43. It can be seen from Fig. 7(a) that the vortex shedding at $D/d = 1.19$ is generally two-dimensional, and the vortex tubes are slightly distorted near the steps. Moreover, the streamwise flow velocity is slower behind the larger cylinder, leading to the upstream bending vortex tubes. At this D/d, the wake vortex modes of larger and smaller cylinders are all characterized by the 2S mode. When $D/d = 1.43$, the vortex tubes are further twisted with the appearance of the streamwise vortices. As shown in Fig. 7(b), although the upstream bending of the vortex tubes appears to more significant, the L-cell and the S-cell are always connected directly. One remarkable point is that the complex spanwise flow and the streamwise vortex derived from the step weaken this coordination so that a "void" appears first in the S-cell downstream of the steps, as indicated by the circles in Fig. 7(b). Subsequently, the "void" gradually spreads to the entire S-cell vortex during the downstream movement of the vortex, splitting the whole S-cell vortex into two parallel parts. At $D/d = 1.43$, the vortex modes behind larger and smaller cylinders present an obvious difference: the larger cylinder

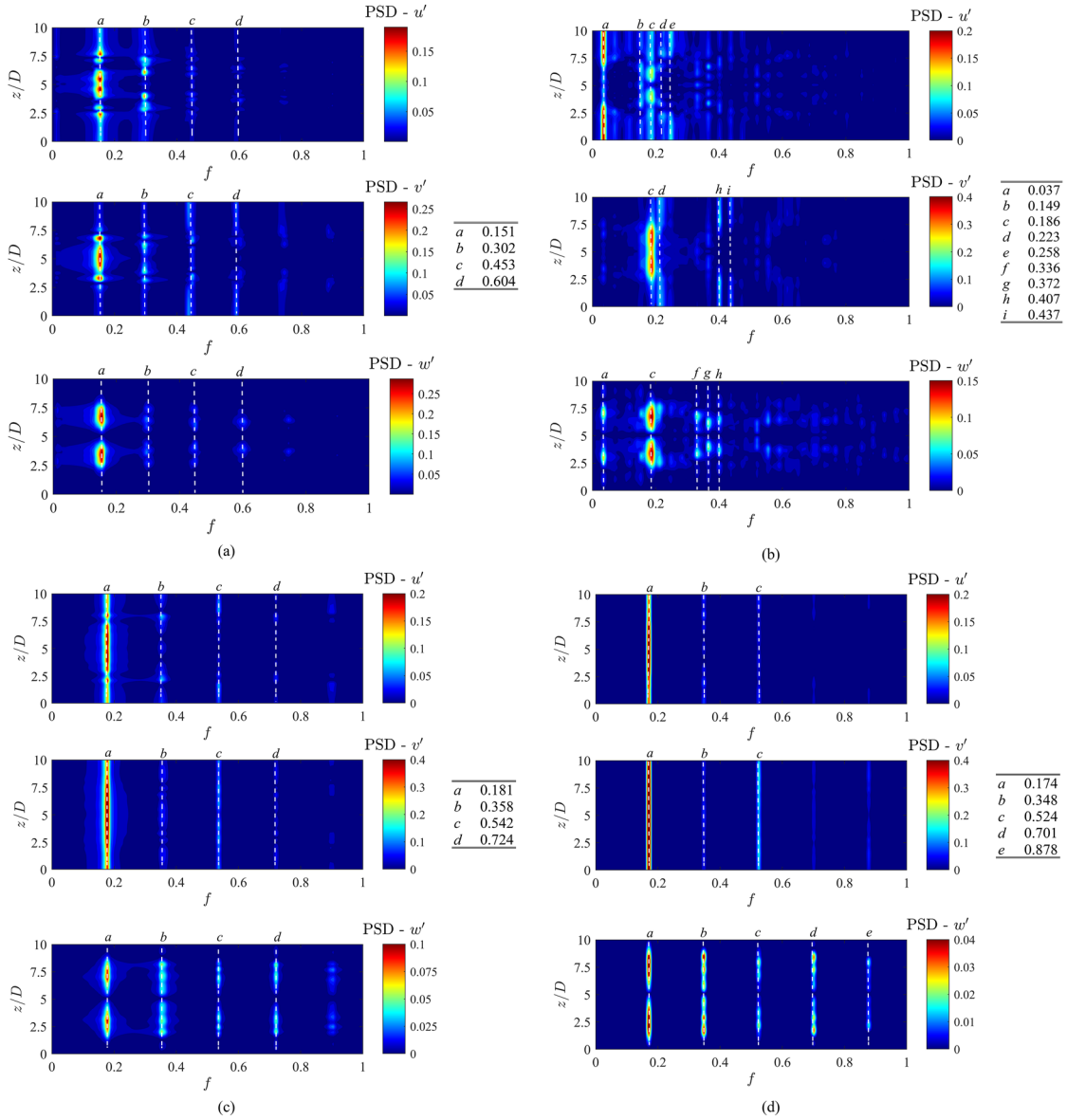

FIG. 6. PSD of velocity fluctuations in three directions at $X/D = 5$ and $Y/D = 0.75$ for four different D/d: (a) $D/d = 4.0$, (b) $D/d = 2.0$, (c) $D/d = 1.43$, and (d) $D/d = 1.19$.

wake remains in the 2S mode, while the 2P mode dominates in the smaller cylinder wake.

The instantaneous isosurfaces of λ_2 at four typical instants in one shedding period of the larger cylinder at $D/d = 4.0$ are selected in Fig. 8, where L-cell vortices downstream the larger cylinder are numbered as +L1, −L1, +L2, −L2, . . ., and the S-cell vortices downstream the small cylinder are numbered as +1, −1, +2, −2, ... To clarify the wake vortices more clearly, the major vortex structures and vortex connection modes corresponding to Fig. 8 are simplified in Fig. 9. Compared with other D/d, vortex tubes behind the larger cylinder appear with a stronger strength and more severe deformation. This deprives from the larger step at this D/d, which leads to a stronger downwash. Hence, more fluid in the smaller cylinder wake floods into the larger cylinder wake, interacting with the shear layers of the larger cylinder, and eventually forming the strongly and increasingly distorted vortices. Due to this complex interaction, the vortex shedding process of the cylinder is delayed, resulting in a lower shedding frequency than that in other D/d cases. From the continuous change in the L-cell behind the larger cylinder, it can be found that L-cell vortices are gradually deformed downstream, forming complicated vortex structures and connections. In the middle of the L-cell, a pair of streamwise center vortices, forming a "U-like" vortex tube, can be

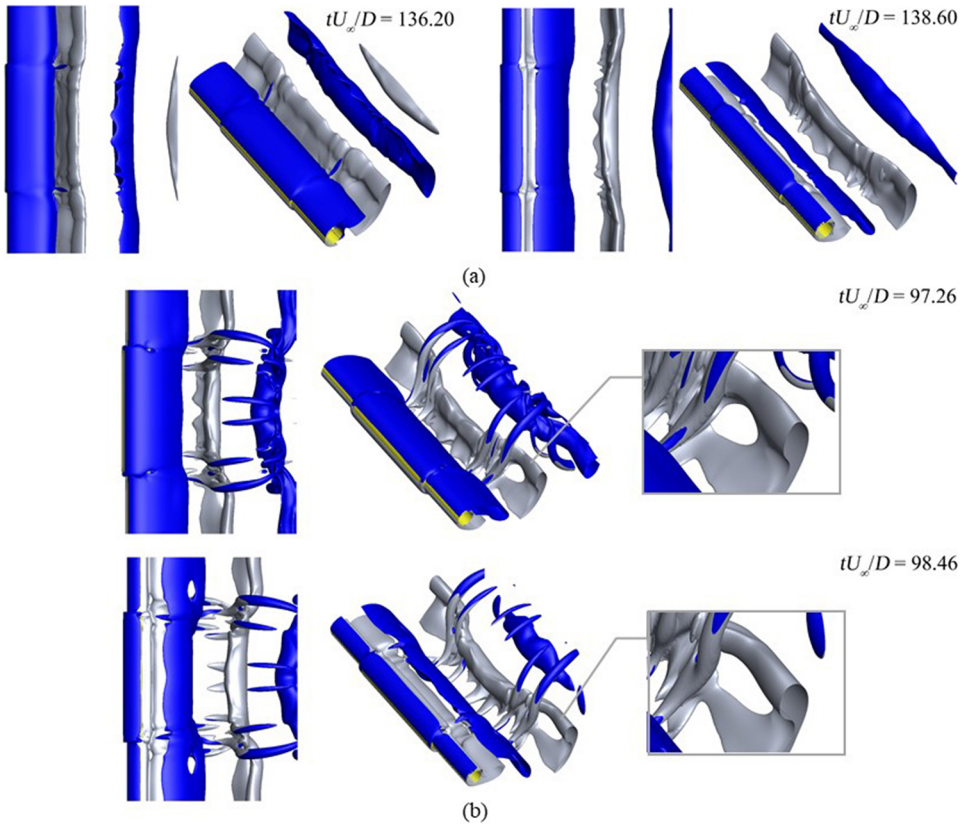

FIG. 7. Instantaneous isosurfaces of λ_2 at two instants with D/d = 1.19 and 1.43: (a) D/d = 1.19 and (b) D/d = 1.43 (silver and blue represent the negative and positive Z-vorticity, respectively).

observed. One possible explanation for the appearance of the center vortices is as follows. The downwash from the steps causes the fluid to be deflected spanwise behind the larger cylinder. The shear layers of the larger cylinder are driven by this spanwise flow during the gradual rolling process to form an axial spiral flow. Then, the axial spiral flow formed at the two steps meets at the larger cylinder center, finally bends, and continues to flow downstream, forming the center vortices (see Fig. 10).

At the boundary of the L-cell and S-cell, L-cell vortices spilt into at least two parts. One part forms a direct connection with an S-cell

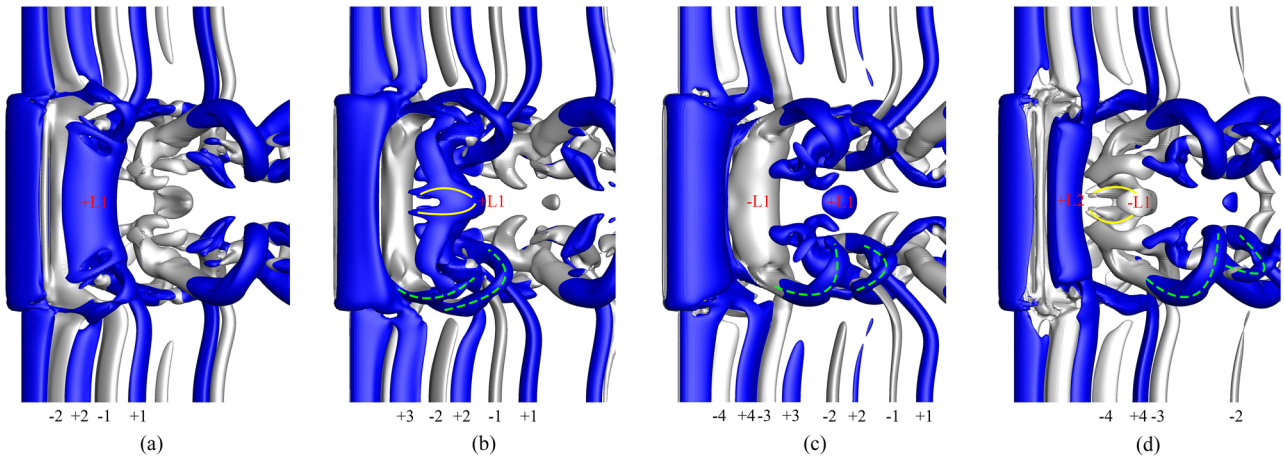

FIG. 8. Instantaneous isosurfaces of λ_2 at four instants at D/d = 4.0: (a) tU_∞/D = 115.4, (b) tU_∞/D = 117.2, (c) tU_∞/D = 119.0, and (d) tU_∞/D = 120.8. (The loop connection between L- and S-cell vortices is indicated by green dashed lines; the yellow solid lines represent a pair of center vortices.)

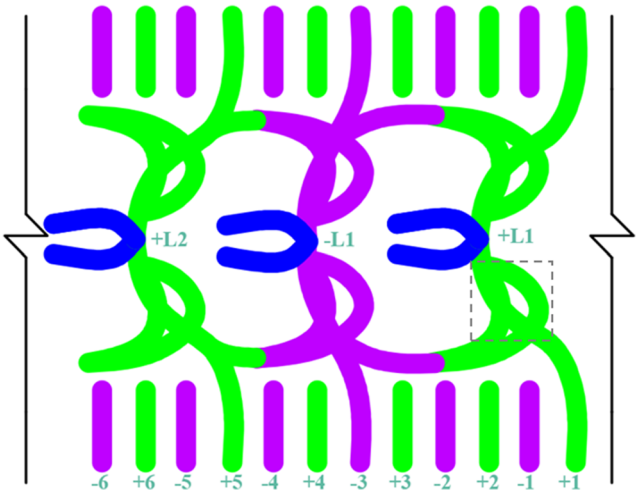

FIG. 9. Simplified vortex connections at D/d = 4.0 corresponding to Fig. 8 (blue solid lines indicate the center vortices; green and purple solid lines denote S-cell vortex; and the loop connection between L- and S-cell vortices is illustrated in the gray dashed box).

of the same sign (+L1 and +1, −L1 and −3). The other part of filaments forms the two loop connections with a subsequent L-cell vortex of opposite sign (+L1 and −L1), which can account for $2f = 0.302$, present downstream of the step on the larger cylinder side in PSD-u'. Behind the smaller cylinder, there exists a phase difference between L-cell and S-cell vortices, caused by the mismatch of the shedding frequency. For this D/d, the shedding phases of smaller and larger cylinders can readjust to a consistent state in one shedding period of the larger cylinder after which a new vortex-shedding-vibration phase realignment process starts.

Instantaneous isosurfaces of λ_2 during tU_∞/D = 141.06–174.06 at D/d = 2.0 are plotted in Fig. 11, where the L-cell vortices downstream the larger cylinder are numbered as +L1, −L1, +L2, −L2, . . ., and the S-cell vortices downstream the small cylinder are numbered as +1, −1, +2, −2, ...

In Fig. 11, the L-cell vortices at different instants exhibit a variety of shapes and different connection modes with the S-cell vortices. For example, the +L2 at tU_∞/D = 144.06 presents a linear shape, the +L4 at tU_∞/D = 159.06 is symmetrically inclined, whereas the −L2

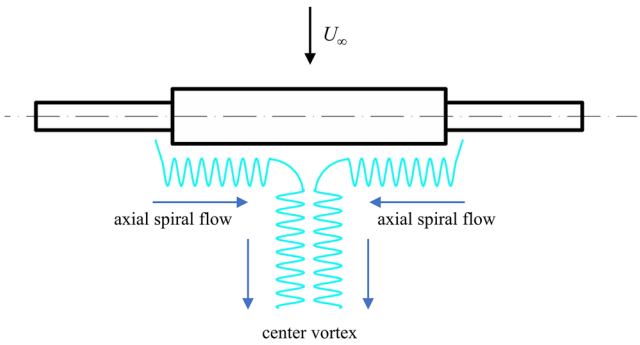

FIG. 10. Sketch of axial spiral flow and center vortex.

at tU_∞/D = 150.06 connects to −3 and −4 simultaneously, forming an "X-shaped" connection. At the downstream of the steps, vortices with opposite phases in the L-cell are always connected to each other by the streamwise vortices: these are caused by the junction and edge vortices[18] generated at the steps. Moreover, a pair of the streamwise center vortices also exists in the middle of the L-cell. By taking the +L4 at tU_∞/D = 156.06 as an example where there is a pair of center vortices at the center of the larger cylinder and near the steps, a streamwise junction vortex connected to +7 and −7 can be observed. A careful scrutinization at Fig. 11 reveals that a unique phenomenon occurs in the vortex shedding of the smaller cylinder: vortices in the S-cell are neither even in the strength nor being shed at a certain frequency. Specifically, in terms of the vortex strength, for example, the strength of the +2 at tU_∞/D = 144.06 is obviously weaker than the surrounding vortices, and this has been too weak to be observed at tU_∞/D = 147.06. Similar phenomenon occurs in the S-cell vortices such as +4, −5, +6, −7, and +8, which are all low in the strength, being invisible in a very close downstream. As for the shedding frequency, by taking the same instant (tU_∞/D = 144.06) as an example, +1 overlaps −1, while +2 and −2 are far apart from each other, demonstrating that S-cell vortices are no longer shed at a specific frequency. This is consistent with results in the velocity fluctuations spectra at D/d = 2.0, where the vortex shedding frequency behind the smaller cylinder has multiple comparable peaks (Fig. 6).

For convenience in the analysis of wake variations, the major vortex structures and vortex connection modes at D/d = 2.0 are simplified in Fig. 12. In Fig. 11, the isosurfaces of λ_2 at tU_∞/D = 141.06 and tU_∞/D = 168.06 are almost identical, indicating that the fundamental dislocation period in which the vortex phase alignment is repeated is approximately tU_∞/D = 27, consistent with the long period of the velocity fluctuations in Fig. 5. In Fig. 12, the wake vortex change from +1 to −11 represents such a long period. During this period (+1 to −11), a total of 5 pairs of L-cell and 11 pairs of the S-cell appear, and the vortex shedding frequencies of the L-cell and S-cell obtained are f_L = 5/27 = 0.186 and f_S = 11/27 = 0.407, respectively. Further analysis of the wake vortices over the long period reveals two "X-shaped" connections (−3 and −L2 and −4, +9 and +L5 and +10), four pairs of weak S-cell vortices (+2 and −2, −5 and +6, −7 and +8, +11 and −11), and two single weak S-cell vortices (+4, −9).

Figure 13 plots time histories of in-line and cross-flow displacements (x and y) in tU_∞/D = 141.06–174.06 at D/d = 2.0, and the instants a to l in Fig. 13 correspond to those in Fig. 11, respectively. Referring to Figs. 11 and 13, it is found that when the cylinder moves upstream with a smaller amplitude [four low-amplitude troughs (i)–(iv) in Fig. 13], the S-cell behind the smaller cylinder is weak. For example, the relatively weak −2 vortex is shed at the trough (i) instant which is slightly ahead of the b instant. This is reasonable because the shear rate of the shear layers and also the wake vortex intensity are lower when the cylinder moves upstream with a slower velocity. Similarly, troughs (ii)–(iv) correspond to the weak +4, +8, and +11 S-cell vortices, respectively. On the other hand, the intensity of the streamwise junction vortices downstream the steps at these instants increases significantly. For example, at tU_∞/D = 159.06, the S-cell vortices +8 and −7 are weak, and the corresponding streamwise structures are stronger. It is considered that a portion of the S-cell vortices is absorbed into the streamwise junction vortices at these instants.

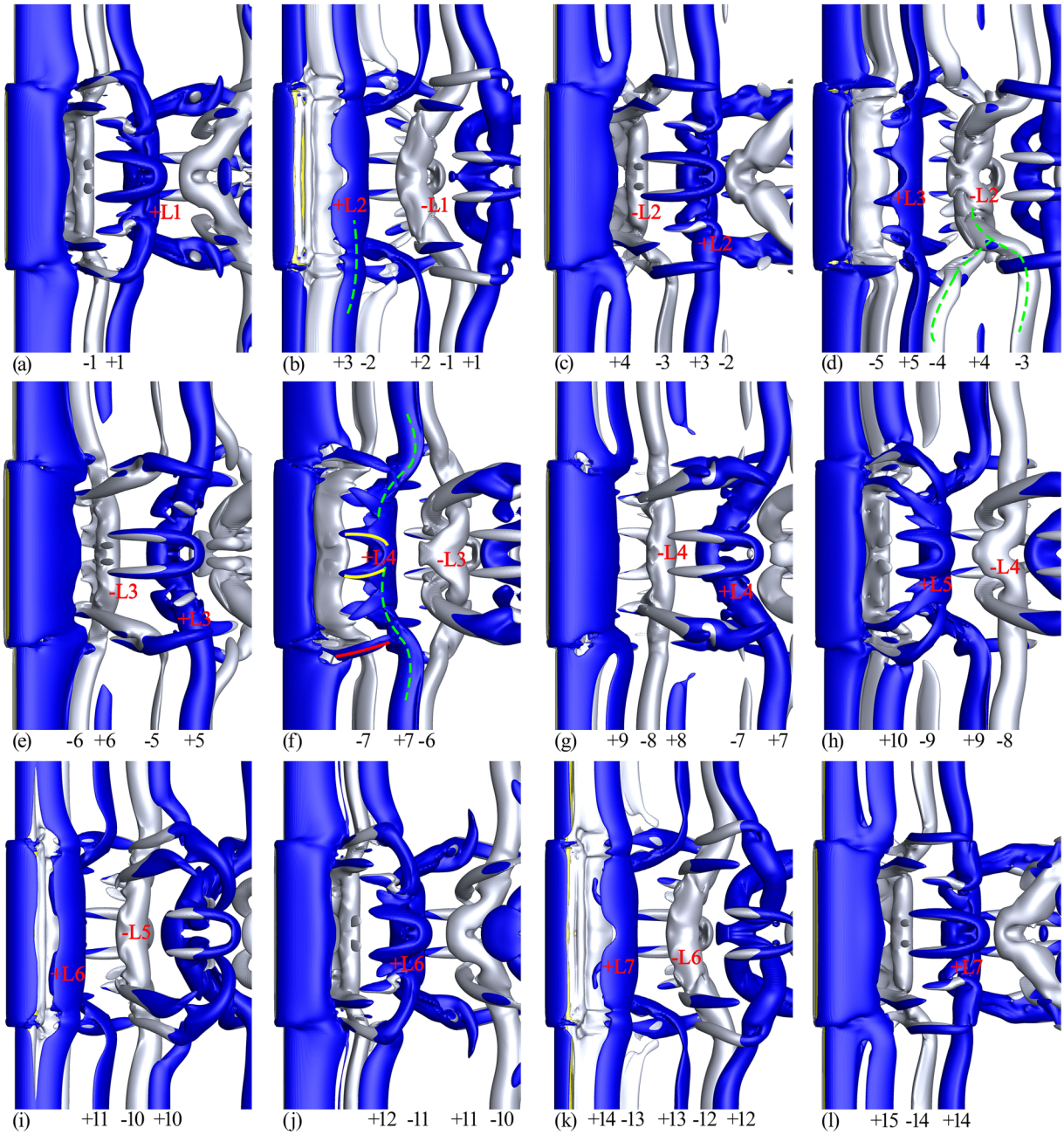

FIG. 11. Instantaneous isosurfaces of λ_2 during tU_∞/D = 141.06–174.06 at D/d = 2.0: (a) tU_∞/D = 141.06, (b) tU_∞/D = 144.06, (c) tU_∞/D = 147.06, (d) tU_∞/D = 150.06, (e) tU_∞/D = 153.06, (f) tU_∞/D = 156.06, (g) tU_∞/D = 159.06, (h) tU_∞/D = 162.06, (i) tU_∞/D = 165.06, (j) tU_∞/D = 168.06, (k) tU_∞/D = 171.06, and (l) tU_∞/D = 174.06. [The different connection modes between L-sell vortices and S-cell vortices in (b), (d), and (f) are indicated by green dashed lines; the yellow solid lines and the red solid line in (f) represent a pair of center vortices and a junction vortex.]

In summary, there are four troughs with smaller amplitudes and the weakened S-cell vortices in a fundamental dislocation period. The frequency is calculated as $f = 4/27 \approx 0.149$, matching the low streamwise vibration frequency at $D/d = 2.0$ in Fig. 4(b). This explains the underlying physics of the low streamwise vibration frequency at $f = 0.149$ as the periodically appeared small-amplitude streamwise vibrations and the associated weakened S-cell vortices. On the other hand, there are also 6 pairs of S-cell vortices with a higher intensity in the fundamental dislocation period (see Fig. 12), and the corresponding frequency is $f = 6/27 \approx 0.223$—one of the

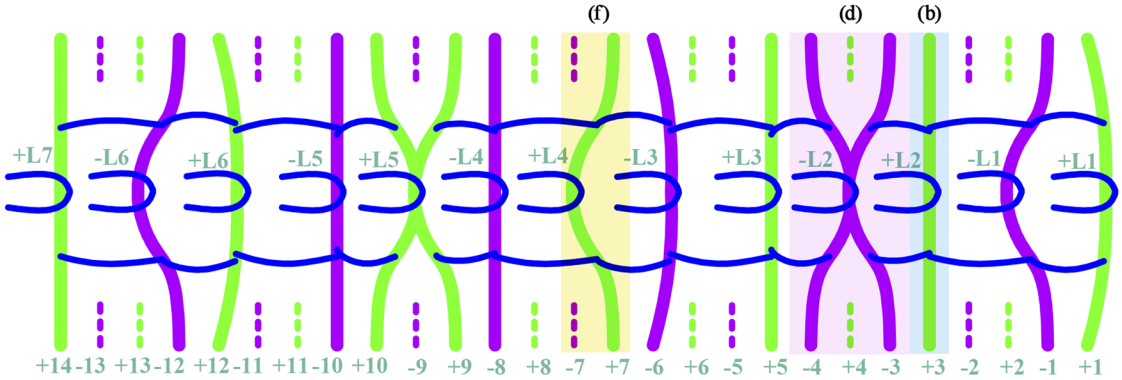

FIG. 12. Simplified vortex connections at D/d = 2.0 corresponding to Fig. 7 [blue solid lines indicate the center and junction vortices (a relatively weak edge vortex is not shown); green and purple solid lines denote strong S-cell vortex; a weak S-cell is represented by thinner green and purple dotted lines; the regions (b), (d), and (f) correspond to the three different vortex connection modes between L-sell vortices and S-sell vortices in Figs. 11(b), 11(d), and 11(f), respectively].

scattered frequencies behind the smaller cylinder in the PSD-u' at D/d = 2.0 [see Fig. 6(b)].

In this paper, the phenomenon that the vortex shedding of the S-cell downstream of the smaller cylinder presenting obvious variations in strength and frequency is called "out-of-phase vortex shedding." To illustrate this point, the selected (Z/D = 1) vorticity fields (ω_Z) at the corresponding instants in Fig. 11 are plotted in Fig. 14. It is seen that S-cell vortices are directly connected to L-cell vortices, exhibiting a classic "2S" mode. For example, the +1 and −1 at tU_∞/D = 144.06, which are equal in strength but opposite in rotation directions, have a regular elliptical shape. The two S-cell vortices that form an "X-shaped" connection with L-cell have a slightly lower vorticity, such as the −3 and −4 at tU_∞/D = 150.06. S-cell vortices that are not connected to the L-cell, such as the +2 at tU_∞/D = 144.06 and the −2 at tU_∞/D = 147.06, are the weakest and present as a strip.

The above observation of the vortex shedding behind the smaller cylinder raises a question regarding the cause of the "out-of-phase vortex shedding" phenomenon. Herein, a reason may be attributed to the mismatch between the smaller cylinder's vortex shedding frequency and the structural vibration frequency. It is seen from the PSD-v' in Fig. 6(b) that the dominant shedding frequency of the larger cylinder is f = 0.186 at D/d = 2.0, while the dominant

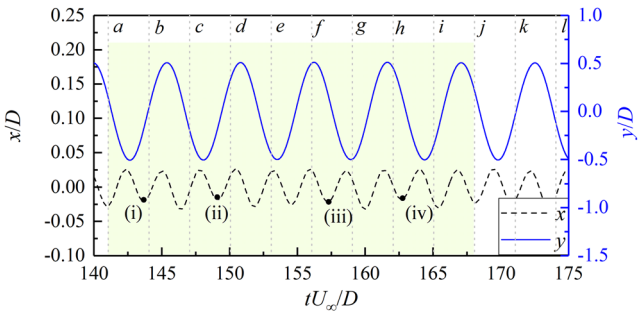

FIG. 13. Time histories of in-line and cross-flow displacements corresponding to Fig. 7 (for in-line displacement, troughs, and crests correspond to the maximum positions upstream and downstream, respectively).

shedding frequency of the smaller cylinder is f = 0.407 with comparable peaks at f = 0.223 and 0.437. The vibration spectrum (Fig. 4) shows that the structural vibration frequencies of both larger and smaller cylinders are f = 0.186. This means that the vortex shedding and cylinder vibration frequencies are locked to each other for the larger cylinder, while the smaller cylinder is not the case. The shedding frequency f = 0.407 that appears behind the smaller cylinder is much higher than the vibration frequency, and this is not an integral multiple of the vibration frequency. The phase lag between the vortex shedding and the cylinder vibration changes continuously with time, and the phase realignment occurs in every fundamental dislocation cycle. Consequently, the phenomenon of "out-of-phase vortex shedding" appears in the S-cell of the smaller cylinder.

According to the wake vortex variation in the fundamental dislocation period in Fig. 12, where the larger and smaller cylinders undergo five and 11 shedding cycles, respectively, the wake vortex structures are completely repeated. The nondimensional time required is tU_∞/D = 27, which is also the vortex-shedding-vibration phase realignment period in the "out-of-phase vortex shedding" mode. The frequency f = 1/27 = 0.037 only appears downstream of the smaller cylinder in the PSD-u' at D/d = 2.0 [Fig. 6(b)], indicating that the "out-of-law vortex shedding" is a unique characteristic of the smaller cylinder.

To explain this unique phenomenon more specifically, two sinusoidal functions A1 and A2 are given to reflect the vortex shedding of larger and smaller cylinders, respectively. The crests and troughs of the functions represent the shedding instants of the positive and negative vortices, respectively. The initial phases of the two functions are determined according to the vortex shedding timing at the start instant in Fig. 11 as 0.5π and −0.232π for A1 and A2, respectively. The functions are as follows:

$$\mathrm{A1} = \sin(0.186 \times 2\pi \times \mathrm{t} + 0.5\pi);\ \mathrm{A2} = \sin(0.407 \times 2\pi \times \mathrm{t} - 0.232\pi).$$

The interaction of the two vortex shedding functions is illustrated in Fig. 15. When +1 is shed from the smaller cylinder, the close crests of A1 and A2 interact to enhance the intensity of +1 and make this S-cell vortex form a direct connection to +L1. There exists a similar relationship between −1 and −L1. For +2, this S-cell

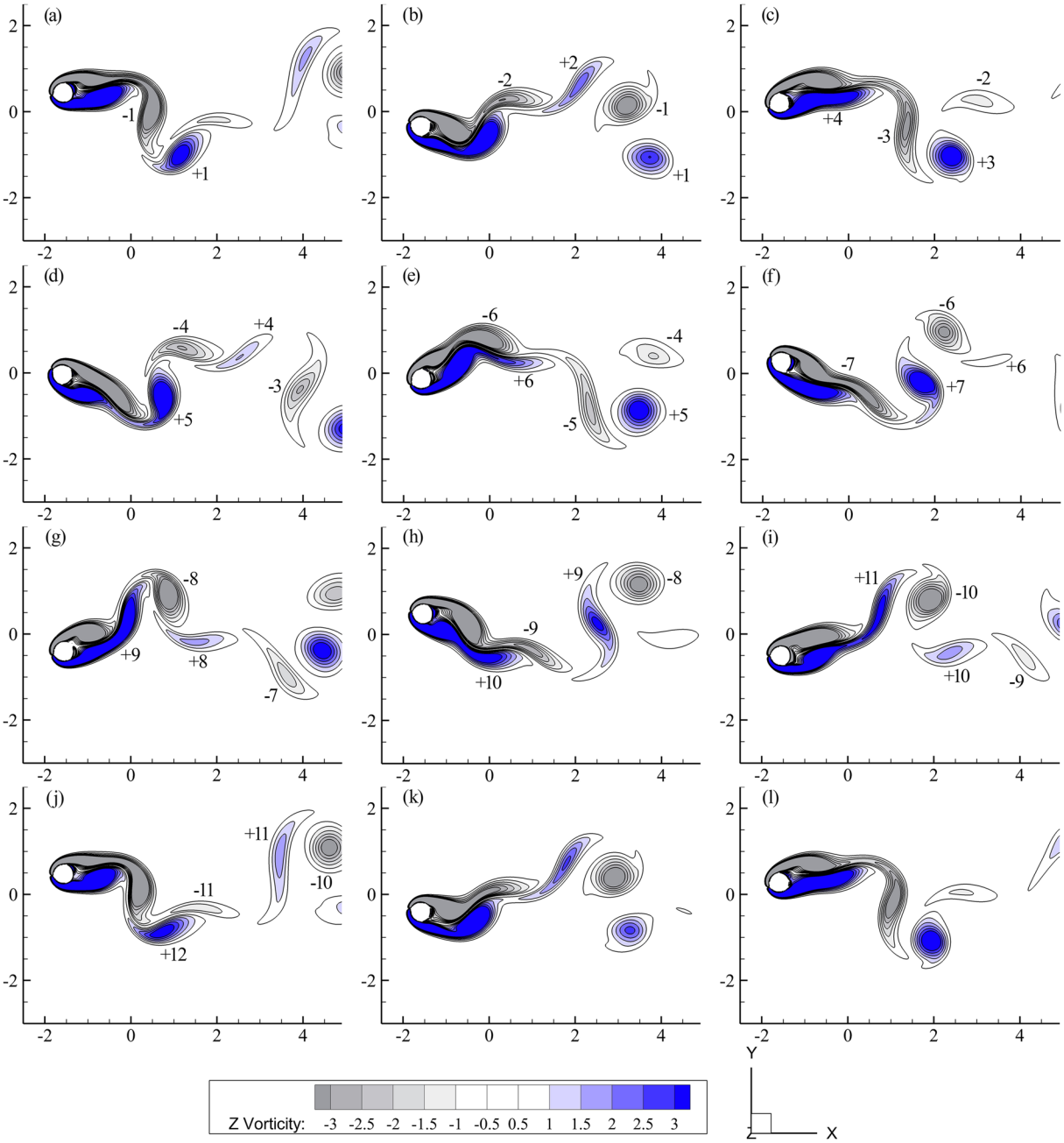

FIG. 14. Vorticity fields (ω_Z) at D/d = 2.0 and Z/D = 1 associated with Fig. 11 for tU_∞/D equal to (a) 141.06, (b) 144.06, (c) 147.06, (d) 150.06, (e) 153.06, (f) 156.06, (g) 159.06, (h) 162.06, (i) 165.06, (j) 168.06, (k) 171.06, and (l) 174.06.

vortex is weakened and is not directly connected to the L-cell due to the antiphase vortex shedding of A1 and A2 at this time. The case of −2 appears to be the same. When the crests of A1 and A2 are close again, the shedding of +3 is stronger and forms a linear direct connection with +L2. For −3 and −4, both A1 and A2 act to cause a negative vortex shedding. However, the trough of A1 is located between the two adjacent troughs of A2, leading to a limited strength of −3 and −4 and an "X-shaped" connection with −L2. The shedding processes of the remaining S-cell vortices are analogized. Hence, the "out-of-phase vortex shedding" phenomenon is essentially identified as a non-lock-in condition between structural vibration and vortex shedding frequencies.

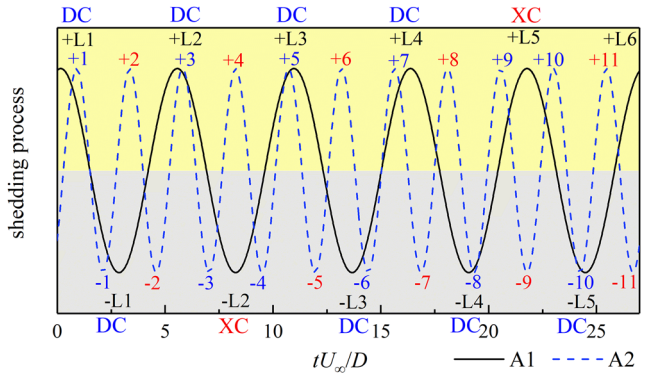

FIG. 15. Interaction of two vortex shedding processes (function curves in yellow and gray background regions denote a positive and negative vortex shedding, respectively; S-cell vortices with higher strength are indicated by blue numbers +1, −1, +3, . . ., and weak S-cell vortices are indicated by red numbers +2, −2, +4, . . .; "DC" and "XC" represents the direct connection and the "X-shaped" connection formed by S-cell and L-cell, respectively).

IV. CONCLUSIONS

VIV of dual-step cylinders with different diameter ratios and a low mass ratio in uniform flows is carried out through direct numerical simulations. The dual-step cylinder is composed of two cylinders with different diameters: a larger diameter (D) cylinder with a length of $5D$ is fixed coaxially at the midspan of a smaller diameter (d) cylinder with a length of $10D$. Four selected diameter ratios are $D/d = 4.0$, 2.0, 1.43, and 1.19. The Reynolds number based on the larger diameter is fixed at 200, whereas that based on the smaller diameter is varied. Key new findings are summarized as follows.

A. Vibration amplitudes

The dual-step change can effectively reduce the cylinder vibration amplitudes. In comparison with the uniform cylinder VIV, cross-flow amplitudes for dual-step cylinders decrease for all the present D/d cases with a greatest reduction at $D/d = 1.43$ of about 19%.

B. Wake vortices

The wake vortices of dual-step cylinders are significantly different from those of a uniform cylinder. Except for $D/d = 1.19$, where vortices exhibit a strong spanwise two-dimensionality, different vortex shedding patterns appear behind both larger and smaller cylinders. Complex vortex connections are also present in the dual-step cylinder wake. For example, a direct and "X-shaped" connection occurs between L- and S-cell vortices at $D/d = 2.0$; a loop connection between two consecutive L-cell vortices appears at $D/d = 4.0$. Besides the spanwise vortices, there are also streamwise vortices such as the junction, edge, and center vortices.

C. "Out-of-phase vortex shedding" phenomenon

When $D/d = 2.0$, the S-cell wake mode shed from the smaller cylinder exhibits a new phenomenon of "out-of-phase vortex shedding" in which the strength of vortices is uneven without a dominant shedding frequency. The root cause for this feature is that the vortex shedding frequency of the S-cell is unlocked with the structural vibration frequency. This distinctive phenomenon also occurs at $D/d = 4.0$, but the vortex shedding frequency of the smaller cylinder appears to be an integer multiple of that of the larger cylinder. The vortex-shedding-vibration phase realignment of the smaller cylinder coincides with the vortex shedding period of the larger cylinder. As D/d decreases to 1.43 and 1.19, the coherence of different cells is enhanced. The vortex-shedding and cylinder vibration frequencies are mutually locked, making the "out-of-phase vortex shedding" disappear.

As a final remark, the present simulations have been carried out based on a spanwise $10D$ domain with the periodic boundary condition. A greater spanwise domain size might lead to different observations. Cases of different spanwise domain scales would be worthwhile for a further study. For the universality of observations, the effects of varying reduced velocity or mass ratio should also be investigated as these parameters are kept constant in this study.

ACKNOWLEDGMENTS

This work was financially supported by the Science Fund for Creative Research Groups of the National Natural Science Foundation of China (Grant No. 51621092) and the National Natural Science Foundation of China (Grant Nos. 51779172 and 51579175). Numerical simulations were performed on TianHe-1(A) at the National Supercomputer Center in Tianjin.

REFERENCES

[1] C. H. K. Williamson and R. Govardhan, "Vortex-induced vibrations," Annu. Rev. Fluid Mech. **36**, 413–455 (2004).
[2] R. Govardhan and C. H. K. Williamson, "Modes of vortex formation and frequency response of a freely vibrating cylinder," J. Fluid Mech. **420**, 85–130 (2000).
[3] A. Khalak and C. H. K. Williamson, "Dynamics of a hydro elastic cylinder with very low mass and damping," J. Fluids Struct. **10**, 455–472 (1996).
[4] A. Khalak and C. H. K. Williamson, "Motions, forces and mode transitions in vortex-vibrations at low mass-damping," J. Fluids Struct. **13**, 813–851 (1999).
[5] T. K. Prasanth and S. Mittal, "Vortex-induced vibrations of a circular cylinder at low Reynolds numbers," J. Fluid Mech. **594**, 463–491 (2008).
[6] T. K. Prasanth and S. Mittal, "Free vs forced vibrations of a cylinder at low Re," Int. J. Comput. Fluid Dyn. **22**(8), 583–592 (2008).
[7] T. K. Prasanth and S. Mittal, "Effect of blockage on free vibration of a circular cylinder at low Re," Int. J. Numer. Methods Fluids **58**, 1063–1080 (2008).
[8] O. M. Griffin and S. E. Ramberg, "The vortex street wakes of vibrating cylinders," J. Fluid Mech. **66**, 553–576 (1974).
[9] O. M. Griffin and S. E. Ramberg, "Vortex shedding from a cylinder vibrating in line with an incident uniform flow," J. Fluid Mech. **75**, 257–271 (1976).
[10] C. H. K. Williamson and A. Roshko, "Vortex for motion in the wake of an oscillating cylinder," J. Fluids Struct. **2**, 355–381 (1988).
[11] F. L. Porta and H. Aref, "Numerical experiments on vortex shedding from an oscillating cylinder," J. Fluids Struct. **22**(3), 327–344 (2006).
[12] J. R. Meneghini and P. W. Bearman, "Numerical simulation of high amplitude oscillatory flow about a circular cylinder," J. Fluids Struct. **9**, 435–455 (1995).
[13] M. Raissi, Z. Wang, M. S. Triantafyllou, and G. E. Karniadakis, "Deep learning of vortex-induced vibrations," J. Fluid Mech. **861**, 119–137 (2018).
[14] H. Garg, A. K. Soti, and R. Bhardwaj, "A sharp interface immersed boundary method for vortex-induced vibration in the presence of thermal buoyancy," Phys. Fluids **30**, 023603 (2018).
[15] G. R. S. Assi and P. W. Bearman, "Vortex-induced vibration of a wavy elliptic cylinder," J. Fluids Struct. **80**, 1–21 (2018).

[16]C. Norberg, "An experimental study of the flow around cylinders joined with a step in diameter," in *Proceedings of the 11th Australasian Fluid Mechanics Conference, Hobart, Tasmania, 14–18 December 1992* (University of Tasmania, Hobart, Australia, 1992).
[17]C. G. Lewis and M. Gharib, "An exploration of the wake three dimensionalities caused by a local discontinuity in cylinder diameter," Phys. Fluids **4**, 104 (1992).
[18]W. Dunn and S. Tavoularis, "Experimental studies of vortices shed from cylinders with a step-change in diameter," J. Fluid Mech. **555**, 409–437 (2006).
[19]C. Morton and S. Yarusevych, "Vortex shedding in the wake of a step cylinder," Phys. Fluids **22**, 083602 (2010).
[20]C. H. K. Williamson, "The natural and forced formation of a spot-like 'vortex dislocations' in the transition of a wake," J. Fluid Mech. **243**, 393–441 (1992).
[21]C. Morton and S. Yarusevych, "An experimental investigation of flow past a dual step cylinder," Exp. Fluids **52**, 69–83 (2012).
[22]J. McClure, C. Morton, and S. Yarusevych, "Flow development and structural loading on dual step cylinders in laminar shedding regime," Phys. Fluids **27**, 063602 (2015).
[23]C. Morton and S. Yarusevych, "On vortex shedding from low aspect ratio dual step cylinders," J. Fluids Struct. **44**, 251–269 (2014).
[24]C. Morton, S. Yarusevych, and F. Scarano, "A tomographic particle image velocimetry investigation of the flow development over dual step cylinders," Phys. Fluids **28**, 025104 (2016).
[25]Z. Rao, J. K. Vandiver, and V. Jhingran, "Vortex induced vibration excitation competition between bare and buoyant segments of flexible cylinders," Ocean Eng. **94**, 186–198 (2015).
[26]C. S. Peskin, "Flow patterns around heart valves: A numerical method," J. Comput. Phys. **10**, 252 (1972).
[27]X. Yang, X. Zhang, Z. Li, and G. He, "A smoothing technique for discrete delta functions with application to immersed boundary method in moving boundary simulations," J. Comput. Phys. **228**, 7821–7836 (2009).
[28]H. A. Van der Vorst, "Bi-CGSTAB: A fast and smoothly converging variant of Bi-CG for the solution of nonsymmetric linear systems," SIAM J. Sci. Stat. Comput. **13**, 631–644 (1992).
[29]C. Ji, A. Munjiza, and J. J. R. Williams, "A novel iterative direct-forcing immersed boundary method and its finite volume applications," J. Comput. Phys. **231**, 1797–1821 (2012).
[30]R. Bourguet, G. E. Karniadakis, and M. S. Triantafyllou, "Vortex-induced vibrations of a long flexible cylinder in shear flow," J. Fluid Mech. **677**, 342–382 (2011).